ELSEVIER

Remote Sensing of Environment 78 (2001) 229–238

Remote Sensing of Environment

www.elsevier.com/locate/rse

Delineation of delta ecozones using interferometric SAR phase coherence Mackenzie River Delta, N.W.T., Canada

Cynthia Hall-Atkinson[1], Laurence C. Smith

Department of Geography, University of California, Los Angeles, 405 Hilgard Avenue, Los Angeles, CA 90095, USA

Received 7 April 2000; accepted 3 March 2001

Abstract

Interferometric processing of six C-band synthetic aperture radar (SAR) image pairs for the Mackenzie River Delta shows that phase coherence is more effective than radar backscatter for differentiating willow–alder, spruce, ice, and open water. Similar radar backscattering from vegetation and wind-roughened water surfaces can make such distinctions difficult in SAR backscatter images. In contrast, coherence is preserved over surfaces with rigid scattering elements, such as leafless woody alder, but is lost over temporally unstable surfaces such as open water. We find that willow–alder display highest coherence followed by spruce, frozen lakes and channels, and open water, respectively. This general hierarchy is preserved even when overall image coherence is decreased by increasing temporal and spatial baselines. Evaluation of spatial, thermal noise and temporal components of total observed coherence indicates that temporal decorrelation is a primary control. Short temporal baselines, such as those obtained during the European Remote Sensing Satellite (ERS) 1-day tandem missions, are therefore optimal for obtaining maximum differentiation of surface classes.

1. Introduction

Remote sensing provides timely and cost-efficient means for classifying large or remote wetland ecosystems into biologically significant categories. Sensors such as the Landsat Thematic Mapper (TM) have been used to attain such classifications based upon visible and near-infrared reflectance (Jensen et al., 1986; Mertes, Dunne, & Martinelli, 1996; Ringrose, Matheson, & Boyle, 1988). Synthetic aperture radar (SAR) sensors offer complementary information about surface roughness and dielectric properties, with the additional advantage of cloud penetration. Numerous studies have demonstrated the value of SAR amplitude (radar backscatter) for delineation of wetland ecosystems (Harris & Digby, 1986; Hess & Melack, 1994; Hess, Melack, Filoso, & Wang, 1995; Kasischke & Bourgeau-Chavez, 1997; Krohn, Milton, & Segal, 1983; Pope, Rey-Benalyas, & Paris, 1994; Richards, Woodgate, & Skidmore, 1987). However, the single frequency and fixed polarization of the first and second European Remote Sensing Satellites (ERS-1 and ERS-2) often inhibit differentiation of wetland ecozones because wind, turbulence, and ice can yield backscatter values similar to those of surrounding land surfaces or flooded forests (Smith, 1997). We demonstrate the value of SAR interferometry for discriminating wetland surface types by utilizing interferometric coherence between repeat-pass ERS SAR images. Previous investigations have used interferometry for forest mapping (Askne, Dammert, Ulander, & Smith, 1997; Engdahl & Hyyppä, 1997; Hagberg, Ulander, & Askne, 1995; Ribbes et al., 1997; Sarabandi & Lin, 2000; Strozzi & Wegmüller, 1997), change detection (Wegmüller, Strozzi, Farr, & Werner, 2000; Wegmüller & Werner, 1995), geologic mapping (Ichoku et al., 1998), and river studies (Alsdorf, Melack, et al., 2000; Alsdorf, Smith, & Melack, 2001; Smith & Alsdorf, 1998). Here, we use interferometric phase coherence to delineate wetland ecozones on the Mackenzie Delta, N.W.T., Canada, building upon previous studies that use visible/near-infrared satellite data (Dickson & Smith, 1991; Gratto-Trevor, 1996; Mouchot, Alföldi, De Lisle, & McCullough, 1991; Pearce, 1991).

We also evaluate the relative importance of spatial, temporal, and thermal noise contributions to total observed coherence; and quantify the effects of temporal baseline (i.e., the time separation between SAR image acquisitions)

[1] Now at Jet Propulsion Laboratory, 4800 Oak Grove Drive, Mail Stop: 171-264, Pasadena, CA 91109.

0034-4257/01/$ – see front matter
PII: S0034-4257(01)00221-8

on decorrelation rates for differing surface classes. Finally, interferometric estimates of class surface areas are compared with more traditional methods, namely a ground-validated Landsat TM classification and mapping from aerial photographs.

2. Study area

SAR images were acquired over the Mackenzie River Delta near its entry to the Beaufort sea, from approximately 68°N to 69°N and from 133°45′W to 136°W (Fig. 1). The Mackenzie Delta is the largest Arctic delta in North America, covering about 12,000 km^2 (Mackay, 1974) and containing approximately 25,000 lakes (Lesack, Hecky, & Marsh, 1991). Boreal forest, tundra, and wetland communities characterize the area with their distributions controlled by lake elevations and drainage characteristics (Young, 1978). Poplar (*Populus*), feathermoss (*Pleurozium*), and white and black spruce (*Picea*) trees occupy elevated surfaces on the delta. Willow (*Salix*) and alder (*Alnus*) stands are found along levees and lakeshores (Ferguson & Marsh, 1991; Pearce, 1991). White spruce dominates uplands with black spruce found in more poorly drained areas (Pearce, 1991). In this study, we examine the forest/tundra transition zone (Fig. 1), using interferometric coherence to delineate the generalized surface classes "willow–alder" (providing no differentiation between *Salix* and *Alnus*), "spruce" (providing no differentiation among *Picea*), "ice," and "open water."

3. Methodology

3.1. Interferometry

The ERS-1 and -2 satellites operate in a sun-synchronous orbit at an altitude of approximately 785 km. SARs on both platforms are C-VV (5.66 cm, vertically polarized) with a nominal incident angle of 23°. Acquired images are 100×100 km and record both amplitude and phase of the signal backscattered to the satellite. Three tandem (1-day repeat) ERS-1 and ERS-2 pairs, two 35-day repeat cycle ERS-2 pairs, and one 70-day ERS-2 pair were acquired over the test site (Fig. 1, Table 1).

Raw signal data from the ERS satellites were processed using the Gamma SAR Processor and Interferometry Software (Wegmüller & Werner, 1997). This software was used to create single-look complex (SLC) images from raw signal data. Processing steps included range compression, autofocusing, and azimuth compression. Following construction of individual SLCs, interferometric coherence between them was calculated. Processing steps included baseline estimation from orbit data, precise SLC coregistration, estimation of interferometric coherence, and 2×10 averaging in range and azimuth. SAR data were geocoded using the flat-Earth assumption. Coherence maps were transformed from range-Doppler SAR coordinates to the Universal Transverse Mercator coordinate system, with a processed pixel spacing of approximately 15 m.

Total observed interferometric coherence ρ_{total} is calculated from two coregistered SLC images as (Eq. (1)):

$$\rho_{\text{total}} = \frac{\langle s_1 s_2^* \rangle}{\left(\langle s_1 s_1^* \rangle \langle s_2 s_2^* \rangle\right)^{\frac{1}{2}}} \tag{1}$$

where s_1 and s_2 are the coregistered complex values from two SLC images; asterisks denote complex conjugation; and angular brackets indicate spatial averaging within a rectangular filter. Determination of ρ_{total} for all values of s_1 and s_2 yields a map of ρ_{total} (Fig. 2). In repeat-pass interferometry, ρ_{total} is dependent on spatial baseline (the physical distance between the two antennae), rotation of the target or baseline convergence, data signal-to-noise ratio (SNR), and temporal changes in the scattering properties of

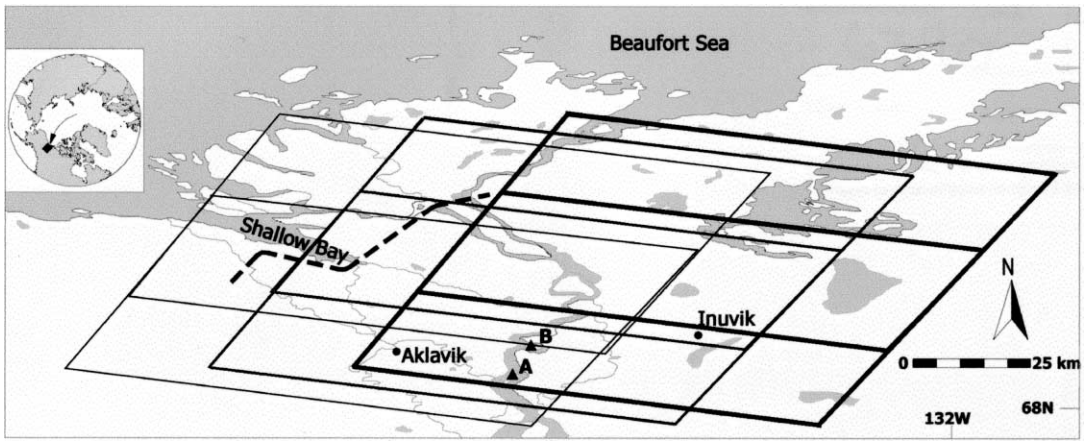

Fig. 1. Location map of the study area, Mackenzie Delta, N.W.T. Boxes represent SAR pairs acquired; different line weights indicate individual pairs. Triangles represent Test Sites A and B used for areal classification. Dashed line represents the transition between the tundra and forest.

Table 1
ERS-1 and ERS-2 SAR image pairs acquired over the Mackenzie Delta

Dates	Orbit	Frame	Temporal baseline (days)	Perpendicular baseline (m)	Parallel baseline (m)
December 15–16, 1995	23105, 03432	2205/2223	1	119	42
January 22–23, 1996	23649, 03976	2205/2223	1	185	91
February 23–24, 1996	24107, 04434	2205/2223	1	110	59
January 27–March 3, 1998	14497, 14998	2205/2223	35	444	159
July 2–August 6, 1998	16730, 17231	2205/2223	35	357	129
December 16, 1995–February 23, 1996	03432, 04434	2205/2223	70	428	208

Time between acquisitions and the perpendicular and parallel components of spatial baseline are also shown.

the imaged surface (Zebker & Villasenor, 1992). As these effects vary between radar acquisitions, decreased accuracy in the measurement of phase leads to a loss of interferometric coherence or "decorrelation." Decorrelation can result from increasing baseline, rapid orbit convergence, low SNR values, and/or changes in the surface over time. Total observed coherence, ρ_{total}, is therefore comprised of baseline ($\rho_{spatial}$), rotational ($\rho_{rotation}$), thermal noise ($\rho_{thermal}$), and temporal ($\rho_{temporal}$) components (Zebker & Villasenor, 1992). The rotational component, $\rho_{rotation}$, is a function of the imaging aspect angle and may be neglected for nearly parallel orbits (Zebker & Villasenor, 1992). For our ERS pairs, calculated baseline convergences were small ($\sim 10^{-3}$°), permitting this term to be dropped, yielding:

$$\rho_{total} = \rho_{spatial} \cdot \rho_{thermal} \cdot \rho_{temporal} \quad (2)$$

The baseline ($\rho_{spatial}$) component may be further subdivided into surface and volume scattering components (Hoen & Zebker, 2000a, 2000b). Separation of these terms requires knowledge of the ratio of volume to surface scattering. Successful modeling of this ratio requires knowledge of the surface scattering structure and attenuation in the canopy, including effective thickness of the scattering layer, canopy surface roughness and penetration depth, the distribution of scattering elements, and an area fill factor representing ground reflections from small open areas between trees (Askne et al., 1997; Hagberg et al., 1995). Because these parameters are not available for our test site, we do not explicitly consider volume vs. surface scattering. These effects are instead lumped in the baseline component ($\rho_{spatial}$) of total interferometric coherence.

In order to assess the relative contributions of $\rho_{spatial}$, $\rho_{thermal}$, and $\rho_{temporal}$, to ρ_{total}, we first computed an average value of ρ_{total} within defined areas where surface characteristics were known. A series of theoretical expressions were then applied to separate the contributions of each component to ρ_{total}. The geometric term $\rho_{spatial}$ was calculated as (Zebker & Villasenor, 1992):

$$\rho_{spatial} = \frac{1 - (2|B|R_y\cos^2\theta)}{\lambda r} \quad (3)$$

with perpendicular baseline B, range resolution R_y, average look angle θ, radar wavelength λ, and distance from the sensor to the center of the resolution element r.

To estimate the amount of decorrelation due only to the spatial baseline effect, the theoretical value of $\rho_{spatial}$ was calculated from Eq. (3) for each image pair. These values were then compared with the observed ρ_{total} for areas in which surficial changes over a short time interval were assumed negligible, thus serving as the closest approximation of decorrelation due only to baseline, i.e., $\rho_{total} \approx \rho_{spatial}$ (Fig. 3). The theoretical critical baseline B_c at which complete spatial decorrelation should occur was computed as (Zebker & Villasenor, 1992):

$$B_c = \frac{\lambda r}{(2R_y\cos^2\theta)} \quad (4)$$

Extrapolation of the observed values of ρ_{total} as a function of baseline yields an observed critical baseline that is slightly lower than the theoretical B_c, indicating that additional, nonspatial sources of decorrelation are also present in these image pairs (Fig. 3). A likely explanation for this difference is the occurrence of minor temporal decorrelation over the 1-day interval between SAR image acquisitions.

To assess the amount of decorrelation attributable to thermal noise of the sensor, values of $\rho_{thermal}$ were calculated using the SNR values from each interferometric pair (Zebker & Villasenor, 1992) (Eq. (5)):

$$\rho_{thermal} = \frac{1}{(1 + \mathrm{SNR}^{-1})} \quad (5)$$

where SNR values were calculated by comparing the average level chirp bandwidth from the signal to the level in the noise only region (Wegmüller & Werner, 1997).

Values of $\rho_{temporal}$ were calculated for willow–alder, spruce, lake and river around Test Sites A and B (Fig. 1) from Eq. (2), using observed values of ρ_{total}, theoretical values of $\rho_{spatial}$, and calculated values of $\rho_{thermal}$ (Table 3). Derived values are plotted for differing surface types in Fig. 4. Note that large temporal baselines ($B_{temporal}$) are associated with reduced $\rho_{temporal}$ for all surface classes.

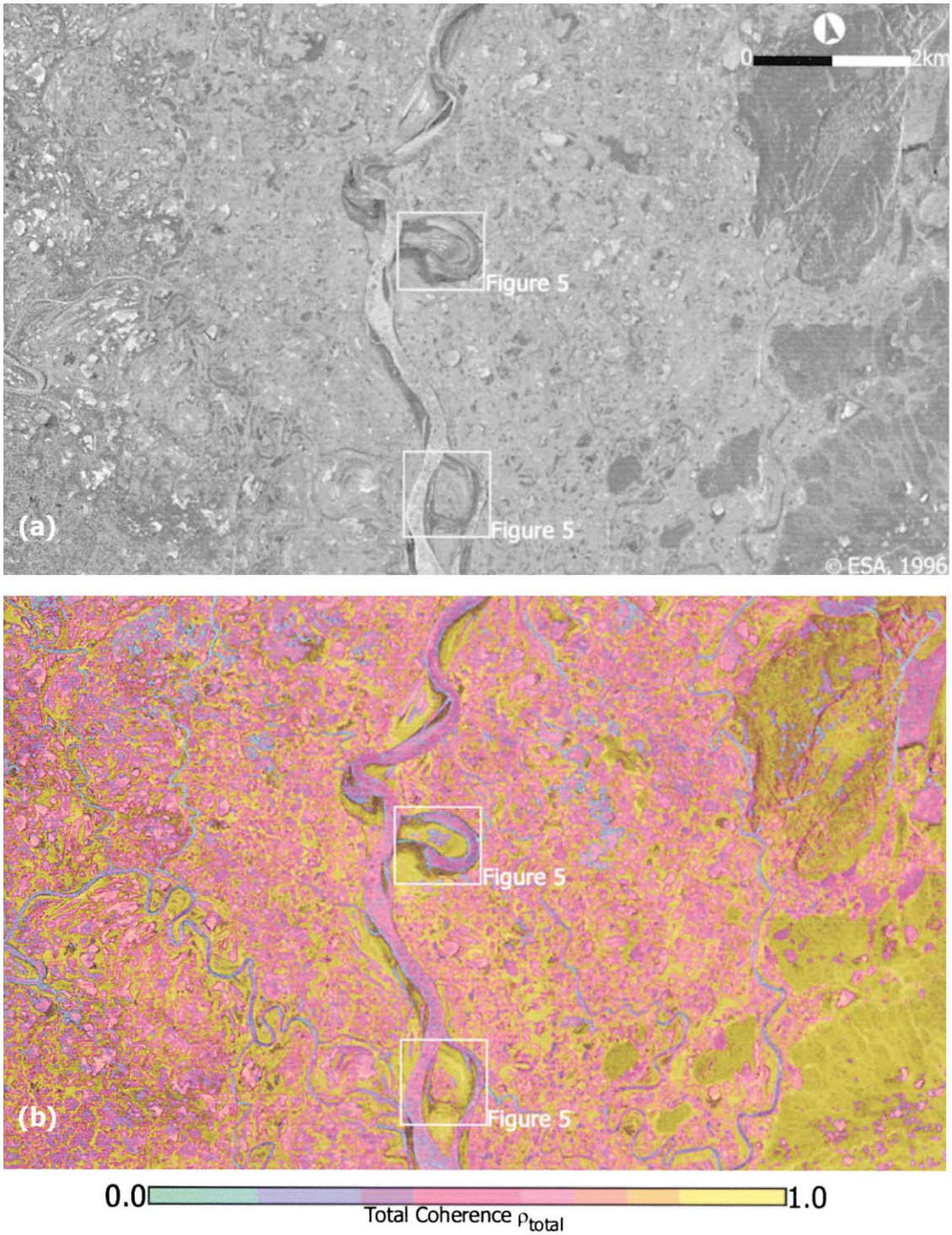

Fig. 2. (a) 24 February 1996 backscatter image and (b) 23–24 February 1996 interferometric phase coherence map of Test Sites A (lower box) and B (upper box). Close-ups are shown in Fig. 5. Yellow represents high coherence and blue represents low coherence; arrow indicates north. Willow–alder stands along the Mackenzie River are difficult to see in the backscatter image (a) but clearly revealed by high coherence in (b).

3.2. Comparison of interferometric results with aerial photography and Landsat TM

Coherence-based estimates of willow–alder area were calculated for Test Sites A and B (Fig. 1) and compared with corresponding estimates from 1985 aerial photographs and a 1994 Landsat TM vegetation classification. Classification thresholds were chosen as the average ρ_{total} value for willow–alder training areas in Sites A and B. Stereoscopy was used to delineate willow–alder from spruce in the aerial photo-

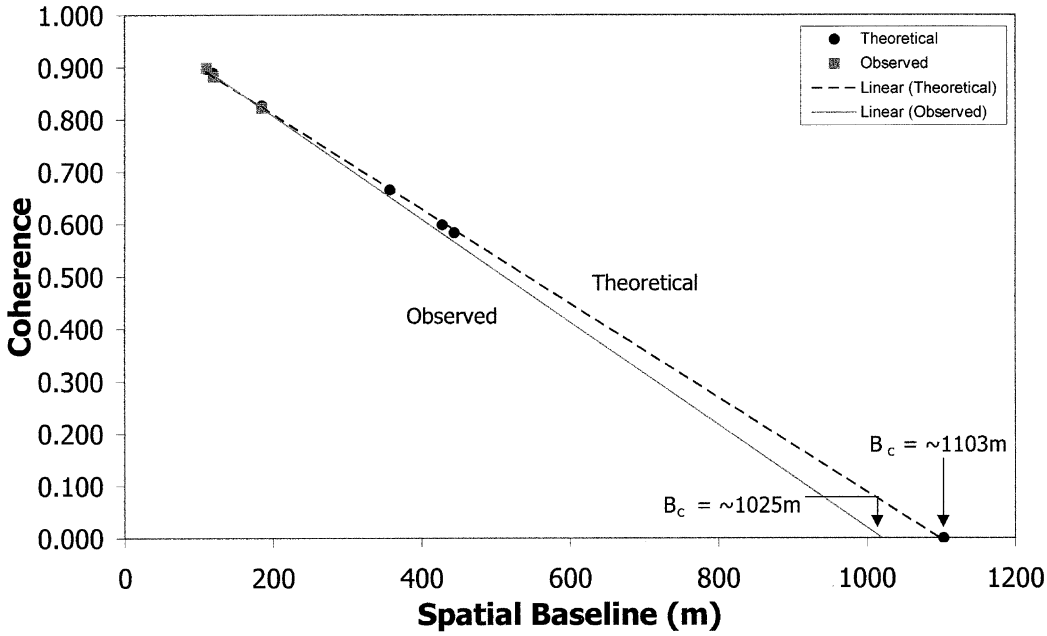

Fig. 3. Observed and theoretical spatial decorrelation (or "baseline decorrelation") for December, January, and February tandem pairs. The difference between observed ($\sim$1025 m) and theoretical ($\sim$1103 m) critical baselines is attributed to temporal and thermal decorrelation.

graphs, based on height differences. Spruce trees in the Mackenzie River Delta are generally several meters taller than willow–alder stands (G. MacDonald, personal communication). This procedure identified sections of predominantly spruce, sections of willow–alder intermixed with a small percentage of spruce and sections of predominantly willow–alder. The density of the stands was determined by tonal variations in the aerial photographs (Fig. 5).

Willow–alder areas were also obtained from a ground-validated Landsat TM (Bands 3, 4, 5) vegetation classification distinguishing 12 similar classes of surface cover. The classification was provided by the University of Western Ontario, Department of Geography. In the present study, classes representing willow–alder subcategories were generalized into three classes for direct comparison with the interferometric classification. Derived areas from aerial photographs, Landsat TM, and six interferometric SAR pairs are presented in Table 4.

4. Results

Interferometric coherence discriminates certain delta surface classes where amplitude alone does not (Fig. 2). Tem-

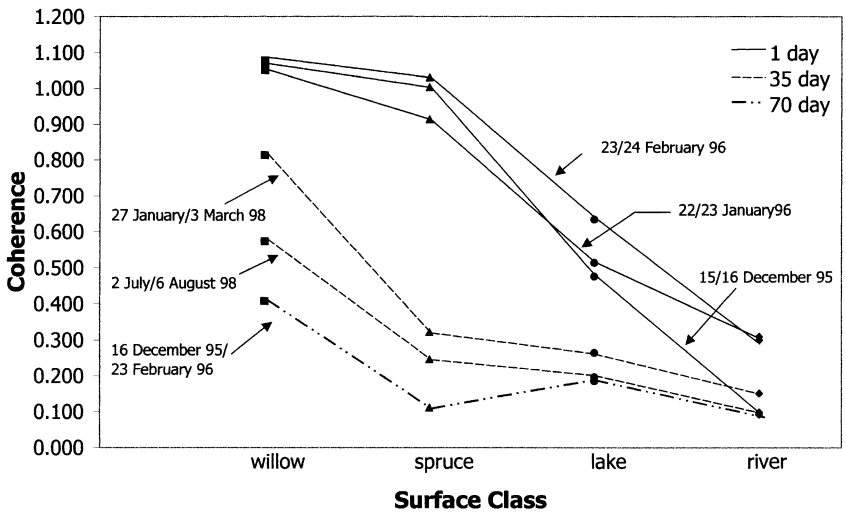

Fig. 4. Temporal decorrelation of surface classes within the Mackenzie Delta. While all classes display decreased coherence with increasing time ("temporal baseline") between image acquisitions, relative coherence levels between classes are preserved. Note that tandem (1-day) image pairs yield highest overall coherence levels and display similar values. Ordinate values are $\rho_{temporal}$; $\rho_{thermal}$ and $\rho_{spatial}$ components have been removed from observed values of ρ_{total}.

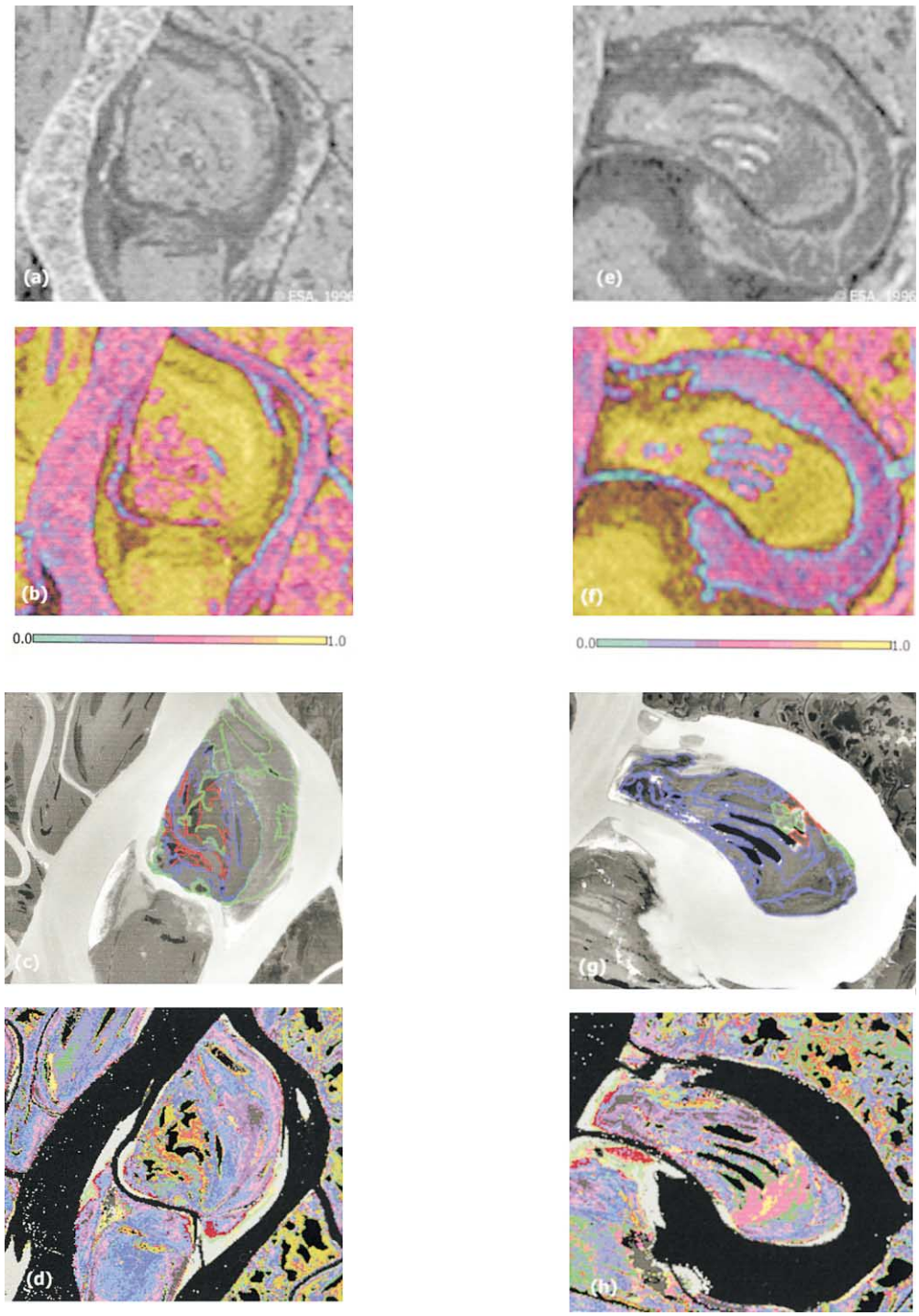

Fig 5. (a–d) Test Site A (68°6.5′N 134°25′W). (e–h) Test Site B (68°14.5′N 134°19′W). (a,e) 24 February 1996 amplitude image. (b,f) 23–24 February 1996 coherence map; color bar shows range of total coherence (ρ_{total}). (c,g) July 1985 aerial photograph delineated by vegetation type. Blue areas represent dense willow and alder stands; green areas represent sparse willow and alder stands; red areas represent spruce intermixed with willow and alder. (d,h) August 1994 Landsat TM classification. Blue and purple areas represent willow and alder stands; green and red represent willow and alder mixed with spruce. Each area is approximately 1×1 km.

poral decorrelation exerts a greater control on total observed coherence than either spatial or thermal decorrelation. Most variations in ρ_{total} are therefore explained by corresponding variations in $\rho_{temporal}$, with highest coherence found where surface scattering elements are rigid (i.e., woody branches) and lowest coherence found where they are not (e.g., free water). These contrasts are useful for discriminating surface classes even where radar amplitudes are similar (Fig. 2).

Table 2
Total observed coherence values over four test sites within the study area

Dates	Perpendicular baseline (m)	Temporal baseline (days)	ρ_{total} — river	ρ_{total} — lake	ρ_{total} — spruce forest	ρ_{total} — willow–alder
December 15–16, 1995	119	1	0.08	0.39	0.82	0.88
January 22–23, 1996	185	1	0.24	0.40	0.71	0.82
February 23–24, 1996	110	1	0.25	0.53	0.86	0.90
January 27–March 3, 1998	444	35	0.08	0.14	0.17	0.43
July 2–August 6, 1998	357	35	0.06	0.12	0.15	0.35
December 16, 1995–February 23, 1996	428	70	0.05	0.10	0.06	0.22

Clear trends in interferometric coherence are found depending on surface type and the length of time between SAR acquisitions (Table 2). Coherence is high over willow–alder, intermediate to high over spruce, low to intermediate over frozen lakes and channels, and low over open water. This relative hierarchy between surface types is preserved even when overall coherence levels are lowered by increasing temporal and spatial baselines. For example, December 15–16, January 22–23, and February 23–24 tandem pairs show coherence values of 0.82–0.90 over willow–alder covered point bars, 0.71–0.86 over the spruce-forested Caribou Hills, and 0.08–0.53 over frozen floodplain lakes and channels (Table 2). January 27–March 3 ERS-2 data show a similar coherence gradient between willow–alder (0.43), spruce (0.17), and ice (0.08–0.14), despite a general reduction in coherence from increased temporal and spatial baselines. Even at 70 days of separation between image acquisitions, willow–alder display the highest coherence (0.22) of any surface class. These observations suggest that relative contrasts in interferometric coherence may be used to distinguish surface classes at a range of temporal and spatial baselines. However, from Table 3, it is clear that increasing temporal baseline significantly reduces overall image coherence levels, a problem mitigated by use of 1-day repeat-pass ERS data.

In addition to surficial change effects, ρ_{total} is seen to decrease with increasing baseline (Table 2). From Eq. (4), the critical baseline at which all coherence will be lost from this effect is 1103 m. To separate spatial from temporal and thermal effects, theoretical values of $\rho_{spatial}$ calculated from Eq. (3) were plotted against observed values of ρ_{total} for areas in which surficial change is assumed negligible over a short time interval (Fig. 3). Values of observed ρ_{total} are thus used as an approximation of $\rho_{spatial}$ over areas with high SNR (minimizing $\rho_{thermal}$) and minimal surficial change (minimizing $\rho_{temporal}$) (Zebker & Villasenor, 1992). Following this logic, ρ_{total} values from high coherence areas within the three winter tandem image pairs were used to produce Fig. 3. Linear extrapolation of observed ρ_{total} values yields an observed critical baseline of approximately 1025 m (Fig. 3). This differs slightly from the theoretical value $B_c = 1103$ m, suggesting that some temporal decorrelation occurs even in high coherence areas. To further identify the effect of temporal decorrelation on total coherence, values of $\rho_{temporal}$ are computed (Table 3) and plotted for different surface classes (Fig. 4). This serves to more clearly display the same trends found in Table 2, but isolates the temporal contribution to ρ_{total}. Values of $\rho_{temporal}$ shown in Table 3 and Fig. 4 differ only slightly from values of ρ_{total} (Table 2). Clearly, temporal decorrelation from surficial change is a primary control on observed variations in ρ_{total}, and drives the hierarchical trends observed between surface classes.

Aerial photographs and a TM-based vegetation classification confirm that high coherence areas correspond to willow–alder stands (Fig. 5). Table 4 compares areas of spruce and willow–alder from Sites A and B (Fig. 1) as derived from coherence mapping, stereoscopy, and Landsat TM. Coherence-based classifications compare well with traditional methods, particularly for short (1-day tandem) temporal baselines. For willow–alder, 1-day coherence

Table 3
Recalculated coherence values for the four test sites in Table 2, attributing all decorrelation to temporal change

Dates	Temporal baseline (days)	$\rho_{temporal}$ — river	$\rho_{temporal}$ — lake	$\rho_{temporal}$ — spruce forest	$\rho_{temporal}$ — willow–alder
December 15–16, 1995	1	0.10	0.48	1.00	1.07
January 22–23, 1996	1	0.31	0.51	0.91	1.05
February 23–24, 1996	1	0.30	0.64	1.03	1.08
January 27–March 3, 1998	35	0.15	0.26	0.32	0.81
July 2–August 6, 1998	35	0.10	0.20	0.25	0.57
December 16, 1995–February 23, 1996	70	0.09	0.19	0.11	0.41

Note similar values to Table 2.

Table 4
Areas of spruce and willow–alder from Test Sites A and B, as estimated from interferometric coherence, aerial photographs, and Landsat TM

Interferometric SAR pair	Perpendicular baseline (m)	Temporal baseline (days)	Coherence threshold	Areas, Region A (ha)	Areas, Region B (ha)
December 15–16, 1995	119	1	0.80		
Willow–alder				14.5	8.7
Spruce				3.7	0.8
January 22–23, 1996	185	1	0.75		
Willow–alder				12.9	8.9
Spruce				3.7	0.6
February 23–24, 1996	110	1	0.80		
Willow–alder				14.9	9.1
Spruce				2.6	0.5
January 27–March 3, 1998	444	35	0.17		
Willow–alder				12.4	8.6
Spruce				4.6	1.3
July 2–August 6, 1998	357	35	0.15		
Willow–alder				11.0	7.8
Spruce				6.6	4.5
December 16, 1995–February 23, 1996	428	70	0.06		
Willow–alder				11.7	7.6
Spruce				5.2	2.4
Aerial photo					
Willow–alder				15.0	9.7
Spruce				2.5	0.4
TM classification					
Willow–alder				15.1	9.9
Spruce				3.0	0.5

One-day tandem SAR pairs agree most closely with traditional methods.

mapping underestimates stereoscopic estimates by 5–15% in Region A and 5–10% in Region B. 35-day coherence mapping in winter underestimates willow–alder areas by about 20% in Region A and 10% in Region B. Larger discrepancies are found in 35-day summer coherence mapping as well as with the 70-day ERS-2 pair. Both underestimate stereoscopic estimates by approximately 30% in Region A and 20% in Region B. Spruce areas are overestimated by 5–20% in 1-day coherence mapping, to as much as 65–90% at 35- and 70-day temporal baselines.

5. Discussion

We find that reduced $\rho_{temporal}$ from surficial change explains most observed losses in ρ_{total}. Within-image variation in $\rho_{temporal}$ is in turn controlled by surface variations in scattering characteristics (Figs. 2 and 4). For all surfaces, further reductions in $\rho_{temporal}$ are introduced by increasing the time between SAR image acquisitions. This effect precludes definition of uniform coherence thresholds for surface classification at all temporal baselines. Therefore, 1-day repeat-pass SAR pairs are recommended for coherence-based classifications.

We propose a phenological explanation for the observed coherence difference between spruce (*Picea*) and willow–alder (*Salix*, *Alnus*) stands. At the scale of the radar wavelength, vegetation structure controls the nature of radar scattering, including its polarization and percentage of volume vs. surface scattering (Leckie & Ranson, 1998). Spruce needles are 15–22-mm long, dense, and remain on branches throughout winter. Willow and alder are deciduous and shed their leaves in autumn, leaving only rigid twigs and branches exposed (Farrar, 1995). During winter, radar energy is therefore backscattered from rigid, woody primary and secondary branches, preserving coherence over time. Spruce evergreen needles are present throughout winter, yielding increased volume scattering and greater spatial and temporal decorrelation. Support for this explanation would be provided by an observation of reduced ρ_{total} from willow and alder during leaf-on conditions. Unavailability of tandem data in summer prevented testing of this hypothesis. Snow accumulation on spruce branches is a second but less plausible explanation, as this phenomenon does not largely influence radar backscatter (Leckie & Ranson, 1998). Coherence contrasts between ice and free water surfaces are readily explained by their rigid vs. moving phase state. However, coherence over ice is still quite low. We attribute this to volume scattering within the snow cover, presence of snowpack structures such as depth hoar and density layering, and/or the presence of bubble structures in ice (Hall, Farge, Klanser, Linebaugh, & Liston, 1994).

6. Conclusions

Interferometric analysis of six ERS SAR image pairs shows that total phase coherence (ρ_{total}) can be used to

distinguish certain surface classes that are not separable in radar amplitude (backscatter) images. Willow–alder stands display highest coherence followed by spruce, frozen lakes, frozen channels, and open water, respectively. This relative hierarchy is preserved even when overall image coherence is reduced from increased spatial and temporal baselines. Evaluation of the spatial, temporal, and thermal noise components of ρ_{total} indicates that temporal decorrelation from surficial change is the greatest contributor to coherence loss. Therefore, SAR image pairs with short temporal baselines, such as 1-day repeat-pass tandem ERS data, are optimal for delineating vegetation and aquatic ecozones in deltaic or wetland environments.

Acknowledgments

Funding for this research was provided by the California Space Institute (project CS-28-97) and the National Science Foundation, Office of Polar Programs, Arctic Systems Science Program (project OPP-9708997). Aerial photographs were provided by the Geological Survey of Canada. The authors thank D.M. Boyes for providing a Landsat TM vegetation classification of the Mackenzie Delta and G.M. Macdonald for useful suggestions. The authors would also like to thank D.E. Alsdorf and two anonymous readers for review of an early version of this paper.

References

Alsdorf, D. E., Melack, J. M., Dunne, T., Mertes, L. A. K., Hess, L. L., & Smith, L. C. (2000). Interferometric radar measurements of water level changes on the Amazon flood plain. *Nature*, *404* (6774), 174–177.

Alsdorf, D. E., Smith, L. C., & Melack, J. M. (2001). Amazon floodplain water level changes measured with interferometric SIR-C radar. *IEEE Transactions on Geoscience and Remote Sensing*, *39* (2), 423–431.

Askne, J. I., Dammert, P. B., Ulander, L. M., & Smith, G. (1997). C-band repeat-pass interferometric SAR observations of the forest. *IEEE Transactions on Geoscience and Remote Sensing*, *35* (1), 25–35.

Dickson, H. L., & Smith, A. R. (1991). Use of Landsat Thematic Mapper and multi-spectral scanning imagery to identify habitats and shorebird nesting areas on the outer Mackenzie River Delta, N.W.T. In: P. Marsh, & C. S. L. Ommanney (Eds.), *Proceedings, Mackenzie Delta: environmental interactions and implications of development, Saskatoon, Saskatchewan, NHRI Symposium No. 4* (pp. 91–106). Saskatoon, Saskatchewan: National Hydrology Research Institute, Environment Canada.

Engdahl, M. E., & Hyyppä, J. M. (1997). Forest inventory using interferometric SAR techniques. In: *Proceedings of the 3rd ERS symposium on space at the service of our environment, Florence, Italy* (pp. 345–350). The Netherlands: Estec, Noodrwijk (ESA SP-414).

Farrar, J. L. (1995). *Trees in Canada*. Ontario: Fitzhenry and Whiteside.

Ferguson, M., & Marsh, P. (1991). Discharge and sediment regimes of lake channel systems in the Mackenzie Delta, N.W.T. In: P. Marsh, & C. S. L. Ommanney (Eds.), *Proceedings, Mackenzie Delta: environmental interactions and implications of development, Saskatoon, Saskatchewan, NHRI Symposium No. 4* (pp. 53–68). Saskatoon, Saskatchewan: National Hydrology Research Institute, Environment Canada.

Gratto-Trevor, C. L. (1996). Use of Landsat TM imagery in determining important shorebird habitat in the outer Mackenzie Delta Northwest Territories. *Arctic*, *49* (1), 11–22.

Hagberg, J. O., Ulander, L. M., & Askne, J. (1995). Repeat-pass SAR interferometry over forested terrain. *IEEE Transactions on Geoscience and Remote Sensing*, *33* (2), 331–340.

Hall, D. K., Fagre, D. B., Klanser, F., Linebaugh, G., & Liston, G. E. (1994). Analysis of ERS-1 synthetic aperture radar data of frozen lakes in northern Montana and implications for climate studies. *Journal of Geophysical Research, [Oceans]*, *99* (C11), 22473–22483.

Harris, J., & Digby-Arbus, S. (1986). The detection of wetlands on radar imagery. In: *Proceedings of the Tenth Canadian remote sensing symposium, Edmonton, Alberta* (pp. 529–543). Ottawa: Canadian Aeronautics and Space Institute.

Hess, L. L., & Melack, J. M. (1994). Mapping wetland hydrology and vegetation with synthetic aperture radar. *International Journal of Ecology and Environmental Sciences*, *20*, 197–205.

Hess, L. L., Melack, J. M., Filoso, S., & Wang, Y. (1995). Delineation of inundated area and vegetation along the Amazon Floodplain with the SIR-C synthetic aperture radar. *IEEE Transactions on Geoscience and Remote Sensing*, *33* (4), 896–904.

Hoen, E. W., & Zebker, H. A. (2000a). Topography-driven variations in backscatter strength and depth observed over the Greenland Ice Sheet with InSAR. In: *Geoscience and Remote Sensing Symposium, Proceedings IGARSS 2000, IEEE 2000 International, 2,* 470–472.

Hoen, E. W., & Zebker, H. A. (2000b). Penetration depths inferred from interferometric volume decorrelation observed over the Greenland Ice Sheet. *IEEE Transactions on Geoscience and Remote Sensing*, *38* (6), 2571–2583.

Ichoku, C., Karnieli, A., Arkin, Y., Chorowicz, J., Fleury, T., & Rudant, J.-P. (1998). Exploring the utility potential of SAR interferometric coherence images. *International Journal of Remote Sensing*, *19* (6), 1147–1160.

Jensen, J. R., Hodgson, M. E., Christensen, E., Mackey, Jr., H. E., Tinney, L. R., & Sharitz, R. (1986). Remote sensing inland wetlands: a multispectral approach. *Photogrammetric Engineering and Remote Sensing*, *52* (1), 87–100.

Kasischke, E. S., & Bourgeau-Chavez, L. L. (1997). Monitoring South Florida wetlands using ERS-1 SAR imagery. *Photogrammetric Engineering and Remote Sensing*, *63* (3), 281–291.

Krohn, M. D., Milton, N. M., & Segal, D. B. (1983). Seasat synthetic aperture radar (SAR) response to lowland vegetation types in Eastern Maryland and Virginia. *Journal of Geophysical Research*, *88* (C3), 1937–1952.

Leckie, D. G., & Ranson, K. J. (1998). Forestry applications. In: F. M. Henderson, & A. J. Lewis (Eds.), *Principles and application of imaging radar: manual of remote sensing* (3rd ed., vol. 2, pp. 440–509). New York: Wiley.

Lesack, L. F. W., Hecky, R. E., & Marsh, P. (1991). The influence of frequency and duration of flooding on the nutrient chemistry of Mackenzie Delta lakes. In: P. Marsh, & C. S. L. Ommanney (Eds.), *Proceedings, Mackenzie Delta: environmental interactions and implications of development, Saskatoon, Saskatchewan, NHRI Symposium No. 4* (pp. 19–36). Saskatoon, Saskatchewan: National Hydrology Research Institute, Environment Canada.

Mackay, J. R. (1974). The Mackenzie Delta Area, N.W.T. *Geological survey of Canada miscellaneous report 23*. Ottawa: Geological Survey of Canada, Department of Energy, Mines and Resources.

Mertes, L. A. K., Dunne, T., & Martinelli, L. A. (1996). Channel-floodplain geomorphology along the Solimoes–Amazon River, Brazil. *Geological Society of America Bulletin*, *108* (9), 1089–1107.

Mouchot, M., Alföldi, T., De Lisle, D., & McCullough, G. (1991). Monitoring the water bodies of the Mackenzie Delta by remote sensing methods. *Arctic*, *44* (Suppl. 1), 21–28.

Pearce, C. M. (1991). Monitoring white spruce communities on the Mackenzie Delta with satellites. In: P. Marsh, & C. S. L. Ommanney (Eds.), *Proceedings, Mackenzie Delta: environmental interactions and implications of development, Saskatoon, Saskatchewan, NHRI Symposium*

No. 4 (pp. 107–120). Saskatoon, Saskatchewan: National Hydrology Research Institute, Environment Canada.

Pope, K. O., Rey-Benayas, J. M., & Paris, J. F. (1994). Radar remote sensing of forest and wetland ecosystems in the Central American tropics. *Remote Sensing of Environment*, *48*, 205–219.

Ribbes, F., Toan, T. L., Bruniquel, J., Floury, N., Syussi, N., Liew, S. C., & Wasrin, U. R. (1997). Forest mapping in tropical region using multitemporal and interferometric ERS-1/2 data. In: *Proceedings of the 3rd ERS symposium on space at the service of our environment, Florence, Italy* (pp. 351–356). The Netherlands: Estec, Noodrwijk (ESA SP-414).

Richards, J. A., Woodgate, P. W., & Skidmore, A. K. (1987). An explanation of enhanced radar backscattering from flooded forests. *International Journal of Remote Sensing*, *8* (7), 1093–1100.

Ringrose, S., Matheson, W., & Boyle, T. (1988). Differentiation of ecological zones in the Okavango Delta, Botswana by classification and contextural analyses of Landsat MSS data. *Photogrammetric Engineering and Remote Sensing*, *54* (5), 601–608.

Sarabandi, K., & Lin, Y.-C. (2000). Simulation of interferometric SAR response for characterizing the scattering phase center statistics of forest canopies. *IEEE Transactions on Geoscience and Remote Sensing*, *38* (1), 115–125.

Smith, L. C. (1997). Satellite remote sensing of river inundation area, stage, and discharge: a review. *Hydrological Processes*, *11*, 1427–1439.

Smith, L. C., & Alsdorf, D. E. (1998). Control on sediment and organic carbon delivery to the Arctic Ocean revealed with space-borne synthetic aperture radar: Ob' River, Siberia. *Geology*, *26* (5), 395–398.

Strozzi, T., & Wegmüller, U. (1997). Forest mapping with ERS SAR interferometry. In: *Proceedings of the 3rd ERS symposium on space at the service of our environment, Florence, Italy* (pp. 357–362). The Netherlands: Estec, Noodrwijk (ESA SP-414).

Wegmüller, U., Strozzi, T., Farr, T., & Werner, C. L. (2000). Arid land surface characterization with repeat-pass SAR interferometry. *IEEE Transactions on Geoscience and Remote Sensing*, *38* (2), 776–781.

Wegmüller, U., & Werner, C. L. (1995). SAR interferometric signature of forest. *IEEE Transactions on Geoscience and Remote Sensing*, *33* (5), 1153–1161.

Wegmüller, U., & Werner, C. L. (1997). Gamma SAR processor and interferometry software. In: *Proceedings of the 3rd symposium on space at the service of our environment, Florence, Italy* (pp. 1687–1692). The Netherlands: Estec, Noodrwijk (ESA SP-414).

F. G., Young (Ed.) (1978). Geological and geographical guide to the Mackenzie Delta area. *CSPG International Conference Facts and Principles of World Oil Occurrence* (pp. 110–121). Calgary, Alberta, Canada: Canadian Society of Petroleum Geologists.

Zebker, H. A., & Villasenor, J. (1992). Decorrelation in interferometric radar echoes. *IEEE Transactions on Geoscience and Remote Sensing*, *30* (5), 950–959.